Journal of Materials Science & Technology 37 (2020) 26–37

Contents lists available at ScienceDirect

Journal of Materials Science & Technology

journal homepage: www.jmst.org

Research Article

Influence of minor Ce additions on the microstructure and mechanical properties of Mg-1.0Sn-0.6Ca alloy

Yanfu Chai[a], Chao He[a], Bin Jiang[a,b,*], Jie Fu[a,**], Zhongtao Jiang[c], Qingshan Yang[d], Haoran Sheng[e], Guangsheng Huang[a], Dingfei Zhang[a], Fusheng Pan[a,b]

[a] State Key Laboratory of Mechanical Transmissions, College of Materials Science and Engineering, Chongqing University, Chongqing, 400044, China
[b] Chongqing Academy of Science and Technology, Chongqing, 401123, China
[c] Research Institute for New Materials Technology, Chongqing University of Arts and Sciences, Chongqing, 402160, China
[d] School of Metallurgy and Material Engineering, Chongqing University of Science and Technology, Chongqing, 401331, China
[e] Shanghai Aerospace Equipment Manufactory, Shanghai, 200245, China

ARTICLE INFO

Article history:
Received 31 May 2019
Received in revised form 10 July 2019
Accepted 15 July 2019
Available online 5 September 2019

Keywords:
Mg-Sn-Ca alloy
Ce content
Microstructure
Texture
Mechanical properties

ABSTRACT

The microstructure and mechanical properties of Mg-Sn-Ca-Ce alloys with different Ce contents (0.0, 0.2, 0.5, 1.0 wt%) were studied at room temperature. Ce additions to ternary Mg-Sn-Ca alloy resulted in grain refinement as well as a change in the category of second phase from CaMgSn to (Ca, Ce)MgSn and $Mg_{12}Ce$. The volume fraction of second phase increased with rising Ce content, which aggravated the restriction of DRXed grain growth during the extrusion process and eventually led to texture weakening of as-extruded Mg-Sn-Ca based alloys. In terms of plasticity, owing to vigorously activated basal slip and homogeneous distributed tensile strain in tension, the tensile ductility of as-extruded alloys reached the maximum value of 27.6% after adding 0.2 wt% Ce, which enhanced by about 26% than that of ternary Mg-Sn-Ca alloy. However, further Ce additions (0.5 and 1.0 wt%) would coarsen the second phase particles and then impair ductility. The tension-compression yield asymmetry of as-extruded Mg-Sn-Ca ternary alloy was alleviated greatly via Ce additions, due to the joint effects of grain refinement, increased amount of strip distributed second phase particles and texture weakening.

1. Introduction

Rising concern has been given to magnesium (Mg) alloys for their light weight, high specific stiffness, satisfactory castability and desirable recyclability [1–5]. However, inadequate strength, poor ductility and strong tensile-compressive yield symmetry (TCA) of wrought Mg alloys all severely hindered their extensive application as construction components [6,7]. Appropriate alloying, as a simple and effective method, can greatly enhance the mechanical performance of Mg alloys via grain refinement, precipitate strengthening and texture modification [8,9]. Among various Mg alloy systems, Mg-Sn based alloys have been stood out and attained constant focus, due to their cost advantage [10], excellent creep resistance [11], loose extrusion conditions [12,13] and so on. Ca element, with an acceptable price, was extensively utilized in Mg alloys to refine grains and weaken texture [14,15]. In particular, Mg-2 wt% Sn alloy though 2 wt% Ca addition owned an extremely high tensile yield strength (440 MPa), because of the submicron grain size (caused by solute Ca element segregations and abundant Mg_2Ca nano-precipitates) [16,17]. Therefore, Mg-Sn-Ca alloy system was a very potential option for the further development of Mg alloys with superior mechanical properties.

In recent years, numerous studies [18–20], concerning the combined addition of Ca and Ce, have been carried out. The main reason was that the double micro-alloying with Ca and Ce could promote the dynamic precipitation and then contribute to strength improvement. As for the Mg-Sn-Ca-Ce alloy system, there only few researches have been recorded [21,22] and the majority of them involved merely in the state of as-cast. Hence, it is imperative to thoroughly assess the role of Ce content on microstructure and mechanical properties of as-cast and as-extruded Mg-Sn-Ca alloy. Consequently, in the current work, the addition of Ce induced grain refinement, second phase transformation and texture weakening

* Corresponding author at: State Key Laboratory of Mechanical Transmissions, College of Materials Science and Engineering, Chongqing University, Chongqing, 400044, China.
** Corresponding author.
E-mail addresses: jiangbinrong@cqu.edu.cn (B. Jiang), fujie3057@cqu.edu.cn (J. Fu).

https://doi.org/10.1016/j.jmst.2019.07.036
1005-0302/

Table 1
Chemical compositions of the as-cast Mg-1.0Sn-0.6Ca-based alloys.

Designation	Nominal alloy	Composition (wt%)			
		Sn	Ca	Ce	Mg
TXE110	Mg-1.0Sn-0.6Ca-0.0Ce	1.31	0.64	–	Bal.
TXE1102	Mg-1.0Sn-0.6Ca-0.2Ce	1.26	0.68	0.14	Bal.
TXE1105	Mg-1.0Sn-0.6Ca-0.5Ce	1.32	0.69	0.53	Bal.
TXE111	Mg-1.0Sn-0.6Ca-1.0Ce	1.29	0.68	1.17	Bal.

were revealed. Besides, mechanical behavior and TCA performance of as-extruded Mg-1.0Sn-0.6Ca-*x*Ce (x = 0.0, 0.2, 0.5, 1.0 wt%) alloys were primarily examined.

2. Experimental procedures

The as-cast Mg-1.0Sn-0.6Ca based alloys having different Ce contents were prepared from commercial high pure Mg (99.85 wt%), high pure Sn (99.90 wt%), Mg-20 wt% Ca and Mg-30 wt% Ce. Four alloy ingots with Ce contents of 0.0, 0.2, 0.5 and 1.0 wt% were produced by melting in an electric-resistance furnace under a mixed protective atmosphere of CO_2 (99%) and SF_6 (1%). The chemical compositions of these alloys were detected by an X-ray fluorescence spectrometer (XRF-1800CCDE) and the relative results were shown in Table 1. Rods (80 mm in diameter and 50 mm in length) cut from the casting ingots, were homogenized at 530 °C for 12 h and then water-cooled. Subsequently, the homogenized samples were hot extruded at 430 °C under a ram speed of 3 mm s^{-1} with an extrusion ratio of 32:1. Microstructural observations were performed by using optical microscopy (OM, ZEISS Axiovert 40 MAT), scanning electron microscopy (SEM, Tescan Vega 3 LMH) equipped with backscattered electron spectrometer (BSE), electron backscatter diffraction (EBSD, JEOL JSM-7800 F) and transmission electron microscopy (TEM, FEI TECNAI G2 F20). For OM and SEM observations, the polished specimens were etched in a mixture of 5 g picric acid, 5 ml acetic acid, 10 ml water and 100 ml ethanol for about 25–30 s. For EBSD inspection, its specimen preparation maintained grinding on SiC papers (grit sizes: 280#, 800#, 1200#, 2000#), washing, blow-drying and subsequently electropolishing in an electrolyte (named AC2) at constant voltage (20 V) and electric current (0.05 A) for 90 s with a temperature of −25 °C. The preparation of TEM sample contained mechanical polishing (~50 μm) as well as ion milling (GATAN, PIPS). The method of linear intercept was adopted to assess the mean grain size (at least 400 grains were included). The volume fraction of second phase particles was measured by the software of Image-Pro 6.0. Five individual SEM pictures were calculated for each alloy, and the ultimate data were averaged. The mechanical properties were tested on a CMT6305-300KN testing machine at room temperature with a strain rate of 1×10^{-3} S^{-1}. Dog bone-shaped tensile specimens (gage length: 14 mm; gage width: 6 mm; gage thickness: 3 mm) and rectangular compressive specimens (gage length: 10 mm; gage width: 8 mm; gage thickness: 3 mm) were both extracted from the alloy sheet along extrusion direction (ED). Each tensile and compressive test was repeated three times to guarantee the accuracy of experiments.

To further uncover the phenomenon that 0.2 wt% Ce addition induced the ductility improvement of as-extruded Mg-Sn-Ca alloy, the corresponding tensile processes (tensile strains of 10% and 20%) were also characterized by EBSD measurements. Meanwhile, in-grain misorientation axes (IGMA) analysis was applied to judge the dominant slip mode (especially for prismatic slip) in deformed grains. The minimum and the maximum misorientation angle for this analysis were taken as 0.5° and 2.0°, separately. Furthermore, crystal plasticity modeling (i.e. VPSC) was employed to ascertain the relative activity of various deformation modes (i.e. slip and twining), thus helping us to understand the difference of stress-strain response between TXE110 and TXE1102 alloys during the tensile process. The viscoplastic constitutive behavior at local level (in a given grain) was described by means of the non-linear rate-sensitivity equation:

$$\varepsilon_{ij}(\bar{x}) = \sum_s m_{ij}^s \gamma^s(\bar{x}) = \gamma_o \sum_s m_{ij}^s \left(\frac{m_{kl}^s \sigma_{kl}(\bar{x})}{\tau_o^s} \right)^n \quad (1)$$

where τ^s (threshold stress) described the resistance for activation that the deformation modes experience and it usually increased with deformation. The code owned the capability of using a reference hardening function for each system, described by an extend voce law (Tomé et al. [23]). As for voce hardening, it was characterized by an evolution of the τ^s with accumulated shear strain in each grain of the form:

$$\tau^s = \tau_0^s + (\tau_1^s + \theta_1^s \Gamma)(1 - \exp(-\Gamma | \frac{\theta_0^s}{\tau_1^s} |)) \quad (2)$$

where $\Gamma = \sum \Delta\gamma^s$ was the accumulated shear in the grain; τ_0^s, θ_0^s, θ_1^s, $(\tau_0^s + \tau_1^s)$ were the initial CRSS, the initial hardening rate, the asymptotic hardening rate and the back-extrapolated CRSS, respectively. The detail theory on VPSC model was described in references [24–28]. And 1000 grains were extracted from the EBSD data with orientations and area fractions.

3. Results

3.1. Microstructural characterization

The OM and BSE SEM micrographs of as-cast Mg-1.0Sn-0.6Ca alloys with different Ce contents are displayed in Fig. 1. It is apparent that the grain size decreases continuously (from ~190.1 μm to ~46.7 μm) and the quantity of second phase increases substantially (from ~9.5% to ~15.9%) with the increase of Ce content. According to the results of EDS, the TXE110 alloy contains α-Mg, CaMgSn phase (needle or short rod-like; as network at grain boundaries) and a few Mg_2Ca phase (sphere-like and tiny particles; distribute within grain), which is in accordance with our previous investigations [29,30]. After adding 0.2 wt% Ce, category and morphology of the second phase is hardly changed, whereas the continuity of its network seems to decrease to some extent. When the content of Ce reaches up to 0.5 wt%, besides Mg, Sn and Ca elements, Ce element is also contained in the needle-like second phase particles, accompanied by the coarsening of their sizes. Second phase exists in TXE111 alloy is still mainly composed of Mg, Sn, Ca, Ce four elements, whereas the ratio between Ce and Ca elements decreases slightly and the morphology of the second phase is more diverse compared to that of TXE1105 alloy.

Fig. 2 provides the microstructural characterization of as-extruded Mg-1.0Sn-0.6Ca-*x*Ce (x = 0.0, 0.2, 0.5, 1.0 wt%) alloys. Evidently, TXE110 alloy owns coarse grains with a mean grain size of ~14.4 μm, whilst for Ce-containing alloy, its relative value decreased gradually (from ~9.5 μm to ~6.4 μm) with rising Ce content. Second phase particles within as-extruded alloys are mainly distributed along the ED in the form of strips, meanwhile the amount of these strips and Ce content are in the direct ratio. Based on the results of EDS, it indicates that Ce additions into Mg-Sn-Ca alloy can bring about the transition of the second phase. Specially, $Mg_{12}Ce$ phase and another new phase containing Mg, Sn, Ca and Ce four elements are appeared in TXE111 alloy when compared with TXE110 alloy. For the sake of further recognize the newly emerged second phase particles in TXE111 alloy, more detailed observations are performed by TEM (see Figs. 3 and 4). As showed in Fig. 3, this quaternary phase possesses two different morpholo-

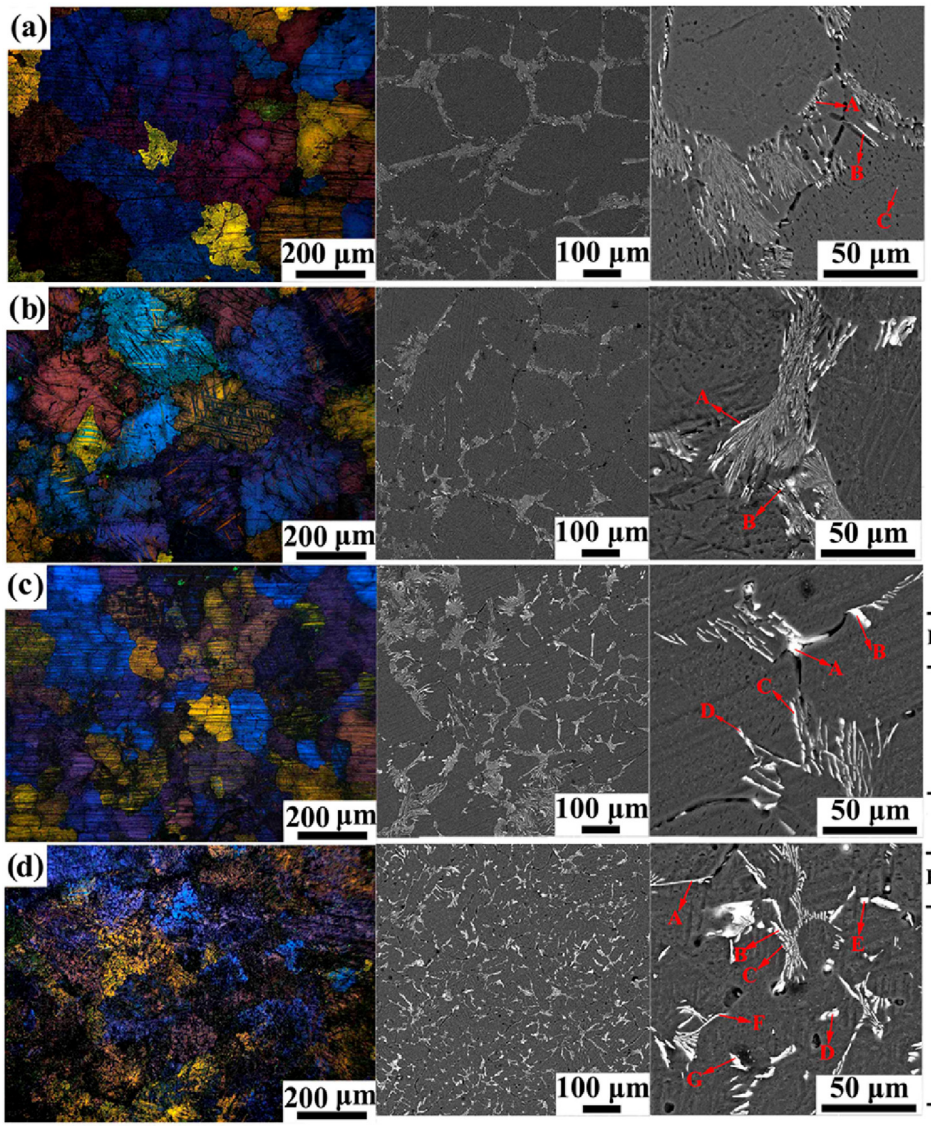

Point	Element (wt.%) Mg	Sn	Ca
A	94.68	4.51	0.81
B	89.34	13.45	2.61
C	99.75	–	0.25

Point	Element (wt.%) Mg	Sn	Ca
A	84.25	13.53	2.22
B	95.87	3.23	0.90

Point	Element (wt.%) Mg	Sn	Ca	Ce
A	83.57	0.09	3.02	13.32
B	90.08	8.17	1.75	–
C	77.08	15.18	2.74	5.00
D	86.34	9.00	1.79	2.87

Point	Element (wt.%) Mg	Sn	Ca	Ce
A	86.83	8.09	2.02	3.07
B	72.95	17.79	3.12	6.15
C	93.20	5.87	0.93	–
D	85.64	10.16	1.79	2.41
E	81.05	12.88	1.83	4.24
F	82.90	10.93	1.80	4.37
G	75.01	15.94	2.71	6.33

Fig. 1. OM and backscattered electron- (BSE-) SEM images of the as-cast Mg-1.0Sn-0.6Ca-based alloys: (a) TXE110 alloy; (b) TXE1102 alloy; (c) TXE1105 alloy; (d) TXE111 alloy.

gies (i.e. irregular block: 0.74–0.94 μm in diameter; rectangular strip: 0.64–2.13 μm in length, 0.22–0.50 μm in width). The TEM-EDX analysis indicates that the content of Mg in this phase is high (possibly disturbed by Mg matrix), meanwhile the atomic ratio among Ca, Ce and Sn elements is close to 1:1:2. Similarly, Kozlov et al. [31] observed the existence of (Ca, Ce)MgSn phase in the quaternary Mg-Ca-Ce-Sn system. Furthermore, they assumed that (Ca, Ce)MgSn phase is composed of CeMgSn (tetragonal system, a = 0.7703 nm, b =0.4628 nm, c =0.9051 nm, with space group P*nma*-62), CaMgSn (tetragonal system, a = 0.786 nm, b =0.466 nm, c =0.874 nm, with space group *Pnma*-62) and Ca_2Sn (tetragonal system, a = 0.9562 nm, b =0.7975 nm, c =0.5044 nm, with space group *Pbnm*-62) phases. The main reason was that CeMgSn phase possesses a very large solid solubility of Ca and serves as a single solid phase up to the known intermetallic solution phase CaMgSn-Ca_2Sn. In the present research, it is worth noting that, compared to that of CeMgSn, the crystal structure of this quaternary second phase is identical (tetragonal system: $\alpha = \beta = \gamma = 90^\circ$), whereas the lattice parameters (a, b and c) exhibit a slight difference (may related to the solid solution of Ca element). In conclusion, combining the corresponding selected area diffractions and the research of Kozlov, this phase (containing Mg, Sn, Ca and Ce elements) can be preliminarily identified as (Ca, Ce)MgSn. As for the $Mg_{12}Ce$ phase (elliptical particle: 0.70–0.80 μm in length, 0.48–0.59 μm in width), its crystal structure is tetragonal system, $a = b$ =1.035 nm, c =0.596 nm, with space group 14/*mmm*-139 [32]. In addition, it is remarkable that Ca element is easily segregated in the vicinity of $Mg_{12}Ce$ phase (refer to the EDS mapping in Fig. 4). As a result, it reflects that the second phase particles of Mg-Sn-Ca alloy have converted from CaMgSn to (Ca, Ce)MgSn and $Mg_{12}Ce$ with increasing Ce content.

Fig. 5 illustrates the EBSD maps and (0001) pole figures of four as-extruded alloys from the extrusion direction-normal direction (ED-ND) plane. The texture of all alloys is marked by an ED-splitting texture feature, which has been extensively reported in Mg alloys in cases of alloying with Ca element [33,34]. The maximum intensity poles of the four alloys are tilted from the ND to ED by approximately ± 30.6°, ± 30.2°, ± 34.4° and ± 35.8°, respectively. Moreover, as the Ce content increases, the maximum texture intensity decreases successively from 15.3 to 11.5.

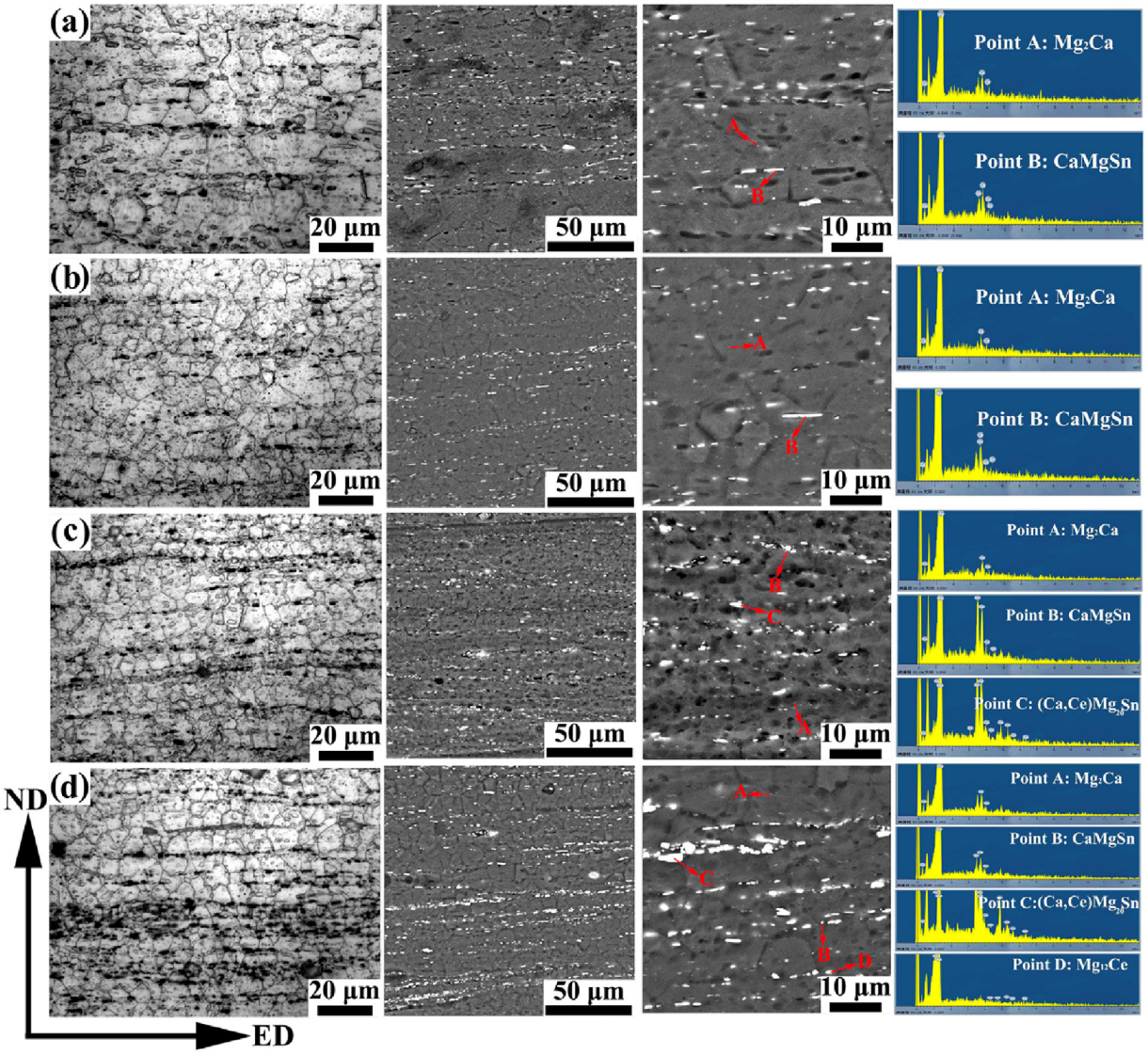

Fig. 2. OM and BSE-SEM images of the as-extruded Mg-1.0Sn-0.6Ca-based alloys: (a) TXE110 alloy; (b) TXE1102 alloy; (c) TXE1105 alloy; (d) TXE111 alloy.

3.2. Mechanical properties

Fig. 6 depicts the true tension and compression stress-strain curves of as-extruded Mg-1.0Sn-0.6Ca-based alloys along the ED. The details of mechanical properties are summarized in Table 2, where tensile yield strength, ultimate tensile strength, compressive yield strength, ultimate compressive strength, elongation to fracture and yield asymmetry are designated as TYS, UTS, CYS, UCS, EL and CYS/TYS, separately. The value of EL in tension increases first and then decreases with increasing Ce content. Especially, the TXE1102 alloy possesses the highest EL (27.6%), enhanced by about 26% than that of TX110 alloy. Comparatively speaking, the EL value in compression is almost constant (21–23%) albeit the variation of Ce content. In terms of strength performance, when the additive amount of Ce element up to 0.5 wt%, both TYS (109.4 MPa) and CYS (93.3 MPa) reach the maximum value, 16.1 MPa and 29.1 MPa higher than TXE110 alloy, respectively. Besides, the increase of CYS originating from Ce additions seems to be greater than that of TYS. In other words, remarkably reduced yield asymmetry of as-extruded Mg-Sn-Ca alloy (CYS/TYS from 0.69 to 0.86) can be implemented by Ce additions.

4. Discussion

4.1. Microstructure variation

The grain size of as-cast Mg-Sn-Ca based alloy decreases monotonously with Ce additions, as shown in Fig. 1. More specifically, the average grain size of TXE111 is only a quarter of that of TXE110. The main reason for the above prominent grain refinement is closely connected with the segregation of solute Ce element [35] and the increase of Ce-containing precipitates [36]. On the one hand, Ce element (2.74; 0.183 nm) owns a higher growth restriction factor and a larger atomic radius than Sn element (1.47; 0.141 nm). Hence, Ce element, with a slow diffusion rate, is easily enriched in the solid/liquid interface during solidification, which eventually leads to constitutional undercooling at the front of the solidification interface [22,37]. On the other hand, due to the very limited solid solubility of Ce element in α-Mg matrix [38], most Ce exists in the form of second phase particles. Therefore, the second phase, which volume fraction increases remarkably with the addition of Ce, also contributes greatly to grain refinement through promoting the nucleation rate and strengthening the ability to pin grain

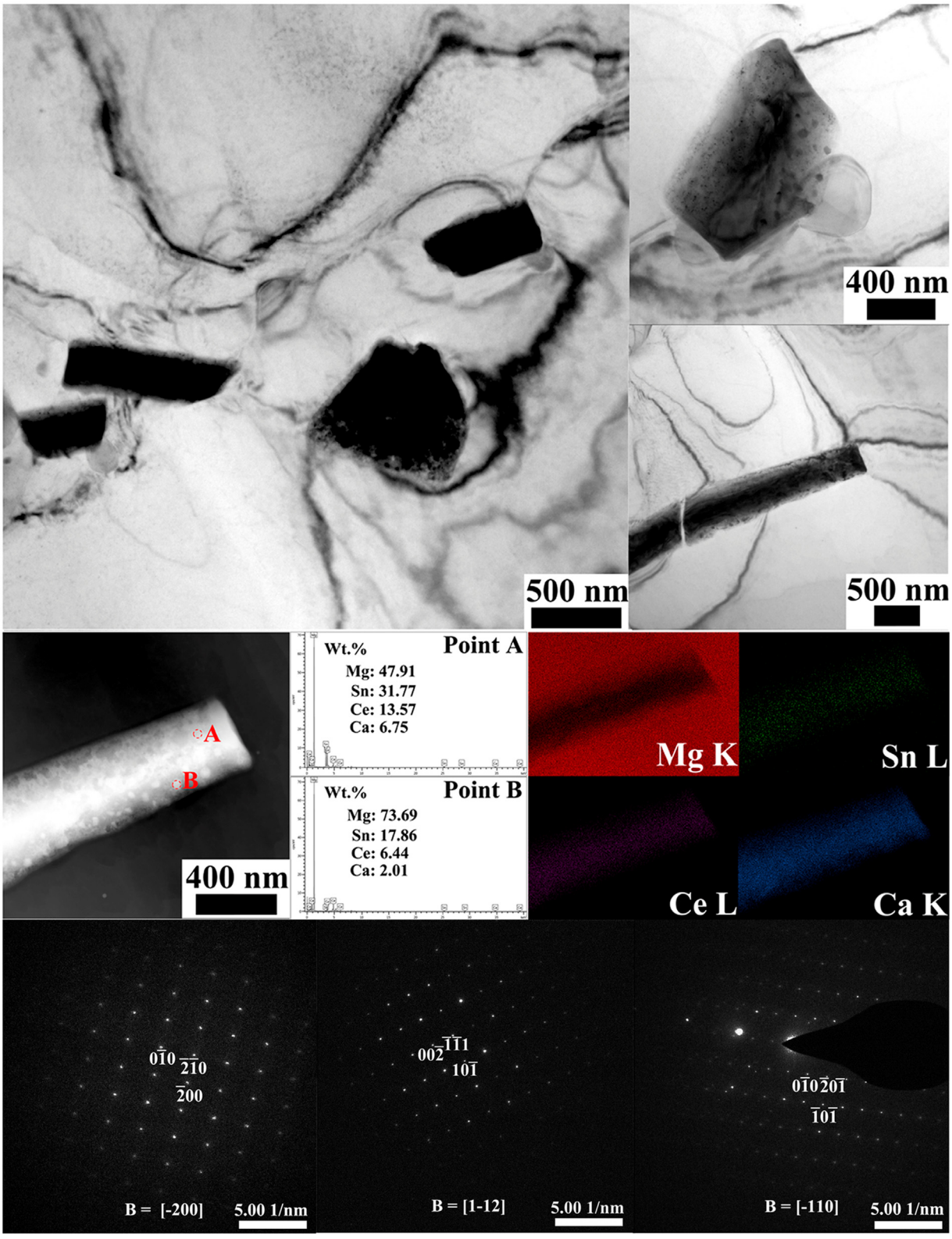

Fig. 3. (Ca, Ce)MgSn phase particles in as-extruded TXE111 alloy sheet.

boundaries. As shown in Fig. 2, the grains of as-extruded alloys keep refining by adding Ce, which is pertained to the combined action of several aspects: (1) the decrease of grain size of as-cast alloy will aggravate the dynamic recrystallization (DRX) during extrusion and then encourage grain refinement. Coincidentally, Barrett et al. [39] also demonstrated that the more initial grain boundaries, the more nucleation positions for DRX during extrusion. (2) second phase particles also play an important role in inhibiting the growth of DRXed grains. In other words, the refinement of grains may be imposed by fragmenting the coarse intermetallic compounds into strips to retard grain growth during extrusion [40]. It is extraordinary apparent from Fig. 2 that the grains adjacent to

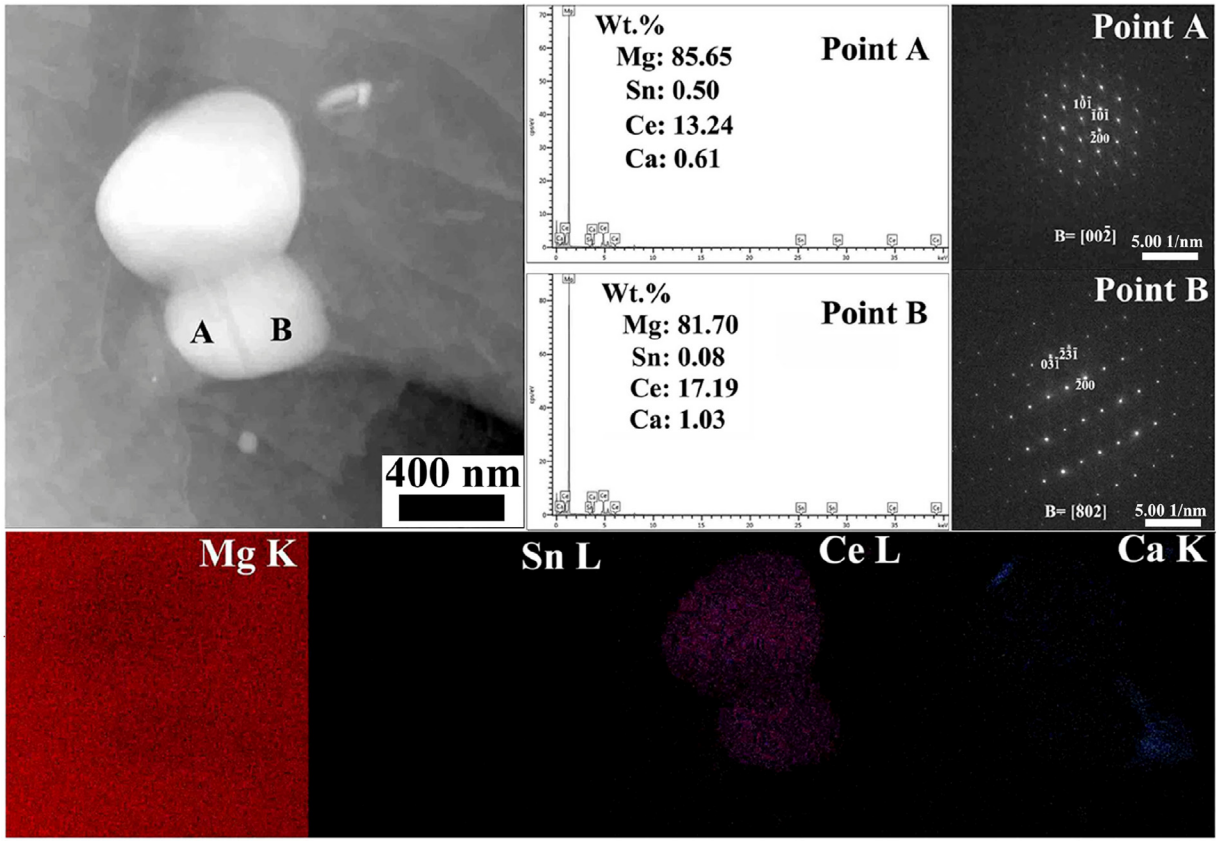

Fig. 4. $Mg_{12}Ce$ phase particles in as-extruded TXE111 alloy sheet.

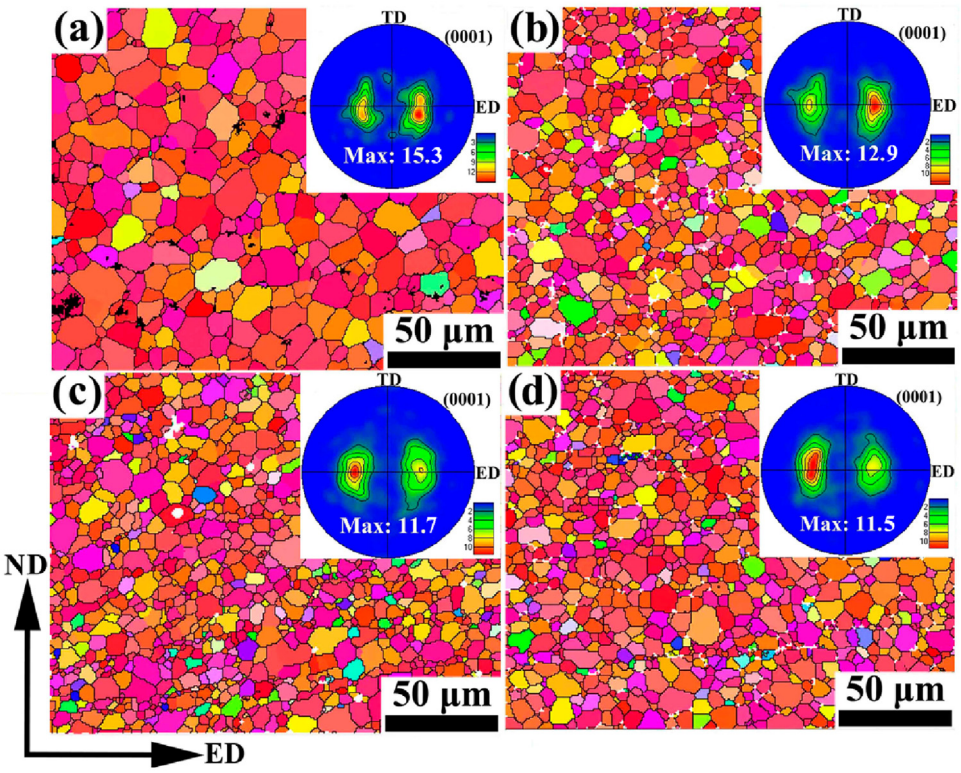

Fig. 5. EBSD inverse pole figure maps and (0001) pole figures from the ED-ND plane of as-extruded Mg-1.0Sn-0.6Ca based alloys: (a) TXE110 alloy; (b) TXE1102 alloy; (c) TXE1105 alloy; (d) TXE111 alloy.

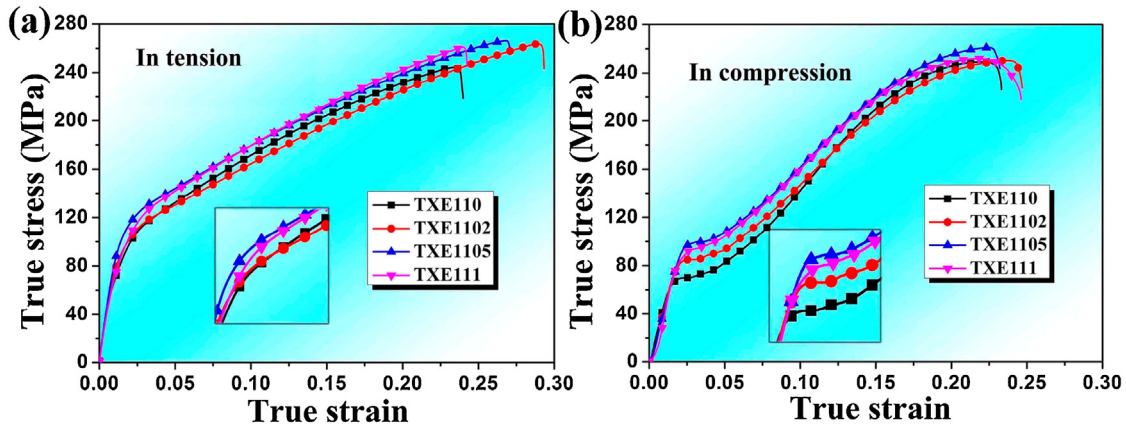

Fig. 6. True tensile and compressive stress-strain curves of as-extruded Mg-1.0Sn-0.6Ca-based alloys: (a) in tension; (b) in compression.

Table 2
Summary of mechanical properties of four as-extruded alloys which suffer from uniaxial tensile and compressive tests along the ED.

Samples	In tension			In compression			CYS/TYS
	TYS (MPa)	UTS (MPa)	EL (%)	CYS (MPa)	UCS (MPa)	EL (%)	
TXE110	93.3	244.6	21.9	64.2	249.2	21.8	0.69
TXE1102	96.8	263.6	27.6	79.4	250.2	22.8	0.82
TXE105	109.4	266.3	25.2	93.3	260.9	23.1	0.85
TXE111	104.2	261.9	22.2	89.8	251.8	22.4	0.86

the second phase particles are much finer than their counterparts in the domain lacking any particles.

As shown in Fig. 5, the addition of Ce into Mg-Sn-Ca alloy can realize the weakening of texture (i.e. decrease of maximum intensity and increase of tilting degree). Resulting from the fact that low solid solubility of Ce element in Mg matrix, hence the above phenomenon is mainly related to the effect of second phase particles on the nucleation [41] and growth [42] of DRXed grains. Fig. 7 presents DRX fraction diagrams of four as-extruded alloys as well as EBSD maps versus different grain sizes. Obviously, almost complete dynamic recrystallization occurred in all samples, which implies that the DRXed grain fraction of the as-extruded Mg-Sn-Ca alloy is independent of additional Ce. Compared with the sample without Ce (TXE110), the proportion of grains smaller than 3 μm (relatively small texture intensity) in the samples containing Ce increased considerably, meanwhile the proportion of grains larger than 12 μm (relatively large texture intensity) decreased accordingly. The above phenomenon reflects that the texture weakening caused by Ce additions may depend on the restriction of grain growth originated from Ce-containing second phase.

4.2. Ce additions induce the variation of ductility

As shown in Fig. 6, among the four as-extruded alloys, the tensile ductility of TXE1102 alloy is the highest (27.6%), which is about 5.7% higher than that of TXE110 alloy (21.9%). To better elaborate the phenomenon that 0.2 wt% Ce addition induces ductility improvement, VPSC and EBSD measurement during the tensile process are performed for both TXE110 and TXE1102 alloys with corresponding results displayed in Figs. 8 and 9, respectively. The extended voce hardening parameters of the four deformation modes are adjusted to the best fit of the experimental stress-strain curves. According to previous studies [26–28], the CRSS of basal slip is located between 5–40 MPa, whereas the CRSS values of prismatic slip and pyramidal slip are about 2–4 times and 5–10 times than that of basal slip, respectively. Besides, for non-basal texture, the ratio of CRSS between basal slip and {10–12} twin ranges from 2:1 to 1:3. As a result, the parameters are empirically defined and listed in

Table 3
Parameters for VPSC constitutive model of as-extruded TXE110 and TXE1102 alloys.

Samples	Modes	τ_0 (MPa)	τ_1 (MPa)	θ_0 (MPa)	θ_1 (MPa)	$h^{ss'}$
TXE110	Basal slip	28	20	200	155	1
	Prismatic <*a*> slip	70	12	500	70	1
	Pyramidal <*c*+*a*> slip	150	100	2800	0	1
	{10–12} tensile twin	40	0	0	0	1
TXE1102	Basal slip	34	4	200	165	1
	Prismatic <*a*> slip	90	5	60	40	1
	Pyramidal <*c*+*a*> slip	130	85	1800	0	1
	{10–12} tensile twin	45	0	0	0	1

Table 3. As shown in Fig. 8, the ultimate results state that the main deformation modes in TXE110 and TXE1102 alloys to accommodate tensile strain are basal slip and prismatic slip. As the tensile strain increases, the relative activity of basal slip decreases persistently, whilst that of prismatic slip increases in turn. Hence, the basal slip dominates the initial stage of deformation, while the prismatic slip can only be involved in the later stage of deformation. The evident discrepancy between TXE110 and TXE1102 alloys is that the intersection point of basal slip and prismatic slip in TXE1102 alloy is relatively delayed comparing to that of TXE110 alloy. In other words, the activation of basal slip in TXE1102 alloy is more vigorous than that in TXE110 alloy during the whole tensile deformation process.

Fig. 9 presents the EBSD measurements of TXE110 and TXE1102 alloys deformed to tensile strains of 10% and 20%. As seen in Fig. 9a and b (tensile strain of 10%), a small amount of {10–12} twins (3%–5%) appeared in the early stage of deformation. Besides, it is no doubt that basal slip can be also activated when tension along the ED, because of the initial ED-splitting texture. According to the research of Hadorn et al. [43], the IGMA distributing at [*uvt*0] could be due to the activation of basal <*a*> slip and pyramidal <*c*+a > slip, while the IGMA appearing in [0001] was caused by the activation of prismatic <*a*> slip. In the current research, the IGMA of both alloys at 10% tensile strain is located at <*uvt*0> (between <10−10> and <2-1-10 >). Hence, the results reflect that for both alloys, the basal

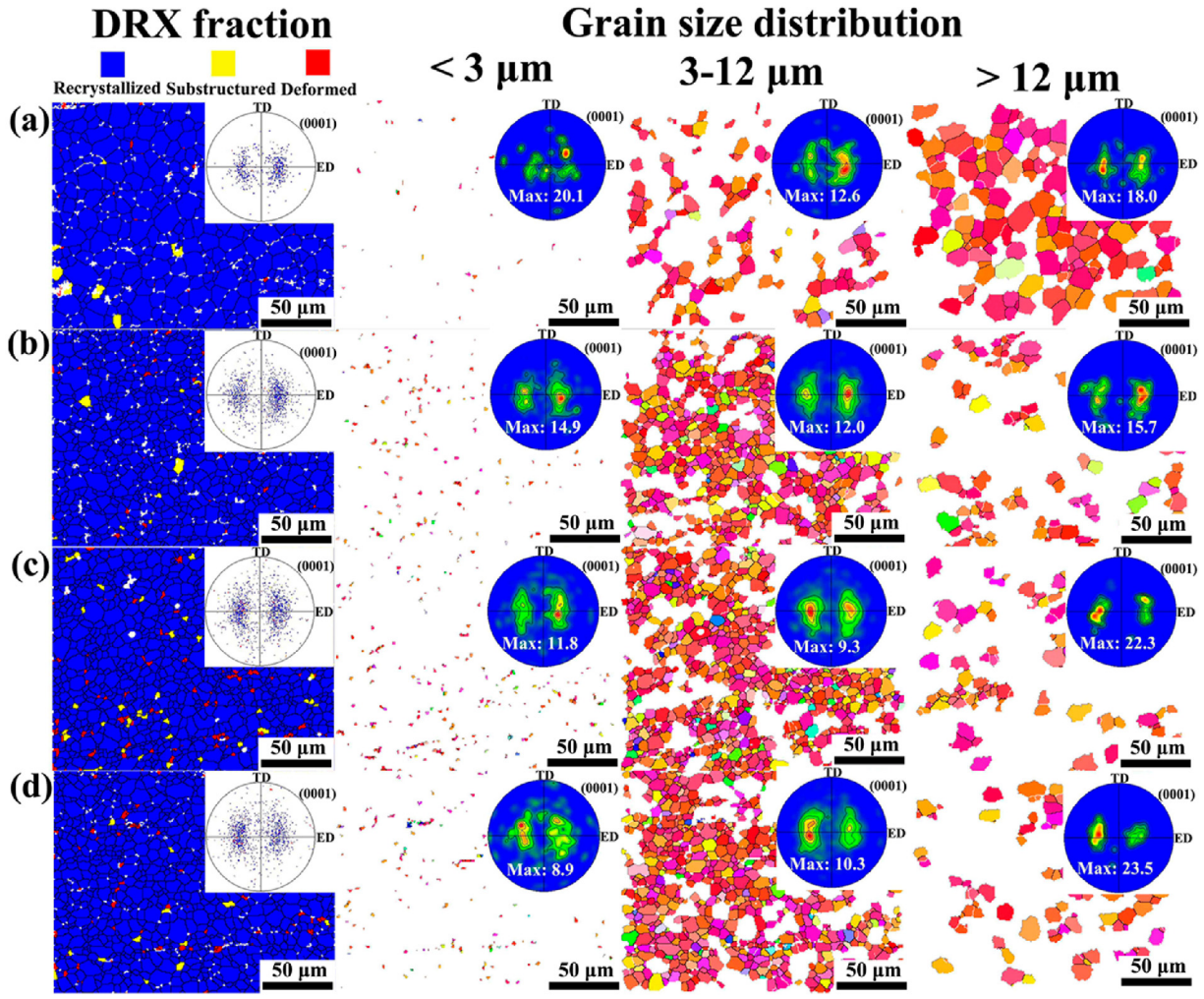

Fig. 7. Different types of grains, EBSD IPF maps in the ED-ND plane and {0001} pole figures of four as-extruded alloys corresponding to grains with size < 3 μm, 3–12 μm and > 12 μm, respectively: (a) TXE110 alloy; (b) TXE1102 alloy; (c) TXE1105 alloy; (d) TXE111 alloy.

slip and {10–12} tensile twins (in the minority) can be activated when the tensile strain is only 0–10%, while the prismatic slip is absent. When the tensile strain reaches 20%, the amount of twins changes little compared to the 10% tensile strain, which implies that no new {10–12} tensile twins are formed between the tensile strain of 10% and 20%. Furthermore, it is noticeable that for TXE110 alloy, the maximum texture intensity (from 10.99 to 7.49) and the tilting degree of maximum intensity pole (from ± 30.09° to ± 25.27°) both decrease after 20% tensile strain compared with 10% tensile strain, whereas the corresponding variation for TXE1102 alloy is not obvious. The decrease of texture intensity and tilting degree is affinitive with the activation of prismatic slip, which is in concurrence with the research of Lee et al. [44]. The above statement is further accentuated by IGMA analysis that the IGMA of TXE110 alloy is partly lying along [0001] at 20% tensile strain. To further shed light on the discrepancy between TXE110 and TXE1102 alloys during the tensile process, Fig. 10 summarizes the distribution of Schmid factor (SF) for basal slip and prismatic slip during tensile deformation. For both alloys, as the tensile strain increases, the SF of basal slip decreases gradually, whereas this decrease degree is more pronounced in TXE110 alloy. In contrast, the SF of prismatic slip increases in turn with increasing strain, while this increase degree between TXE110 and TXE1102 alloys is analogous. Last but not least, on the basis of Kernel average misorientation (KAM) maps (see Fig. 9), it indicates that distribution of tensile strain in TXE1102 alloy is more homogeneous than that in TXE110, whatever the tensile strain of 10% or 20%. As a consequence, improvement of ductility via 0.2 wt% Ce addition is closely associated with the vigorously activated basal slip and homogeneous distributed tensile strain. Unfortunately, the tensile ductility decreases gradually with the further increase of Ce content (0.5 and 1.0 wt%). The possible reason is lying in that excessive Ce additions would coarsen the second phase particles, which can act as crack initiation sites and thus impair ductility [45].

4.3. Reduced tension-compression yield asymmetry through Ce additions

Essentially speaking, the apparent yield asymmetry is derived from the different deformation mechanisms under different loading (i.e. the activation stress required for twinning in compression is lower than that for slip system in tension) [46–48]. The mechanical properties listed in Table 2 declare that the addition of Ce increases the CYS/TYS value of as-extruded Mg-Sn-Ca-based alloys (from the initial 0.69 to 0.82-0.86). The possible reasons for the above phenomenon can be attributed to the following aspects: Firstly, many studies [29,49] have shown that deformation twins were easier to activate in coarse grains than in fine grains (i.e. the reduction of grain size helps to restrain twinning during compression). Furthermore, Dogan et al. [50] expressed that the influence of grain size

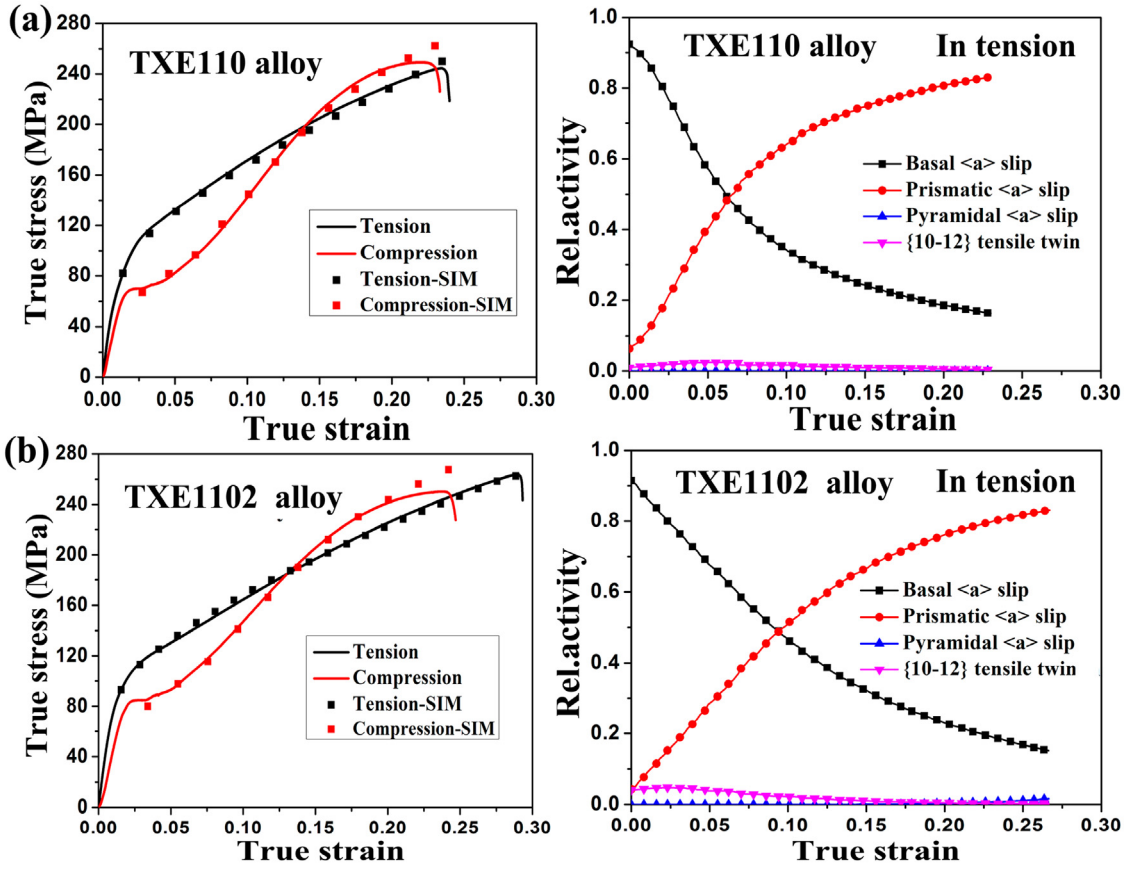

Fig. 8. Experimental (lines) and simulated (symbol) true stress and true strain curves in tension and compression with correspondingly relative activities of different deformation modes in tension: (a) TXE110 alloy sheet; (b) TXE1102 alloy sheet.

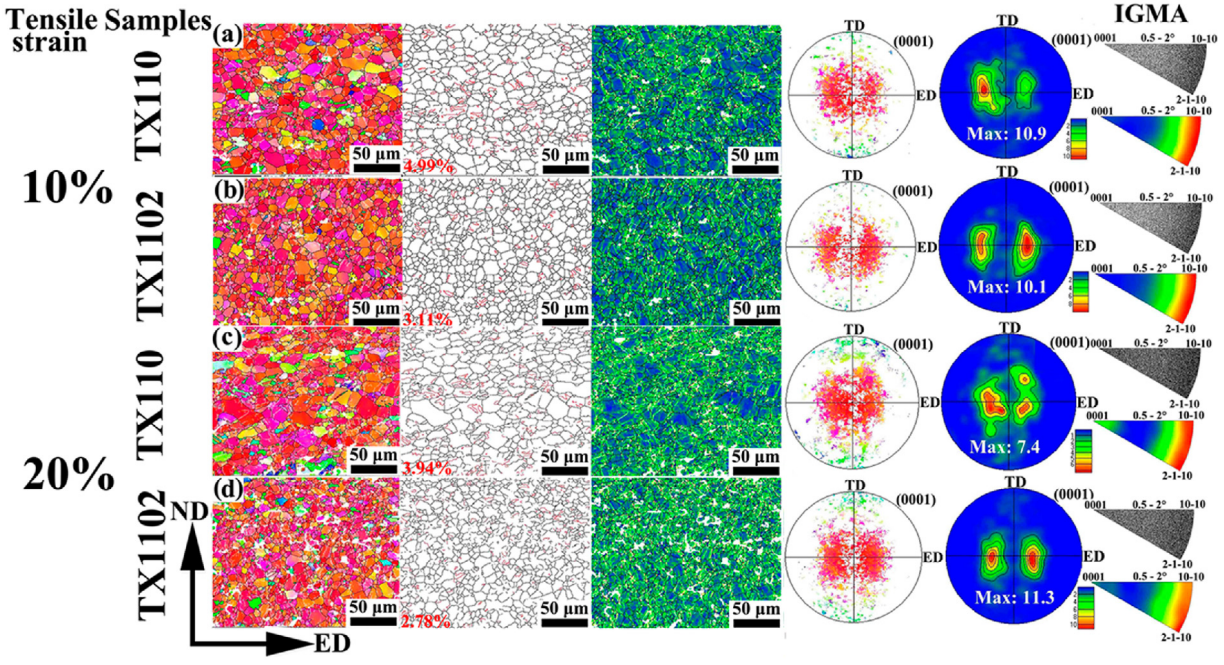

Fig. 9. EBSD measurement results of TXE110 and TXE1102 alloys deformed to tensile strains of (a, b) 10% and (c, d) 20%.

on twining was deemed to greater than that on slip. Hence, grain refinement is regarded as an efficient manner to alleviate TCA. In the present study, Ce additions into the as-extruded TXE100 alloy can induce obvious grain refinement (from 14.4 μm to 6.4 μm). Thus, the improvement of TCA in alloys containing Ce is related to their refined grains. Secondly, it should be emphasized that the precipitates within the grains could pin at the twin boundaries and then suppress the occurrence of twinning by increasing the back stress

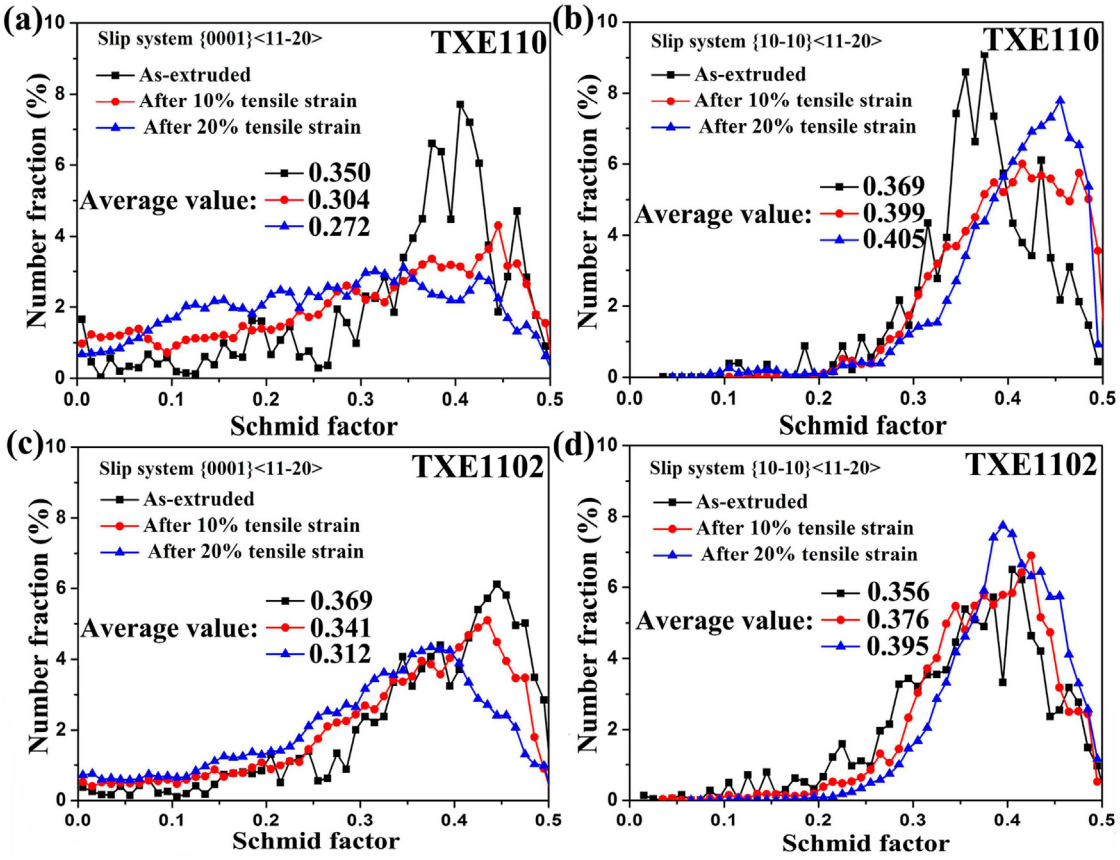

Fig. 10. Quantitative analysis of basal slip and prismatic slip Schmid factor (SF) of the as-extruded TXE110 and TXE1102 alloys during tensile deformation process.

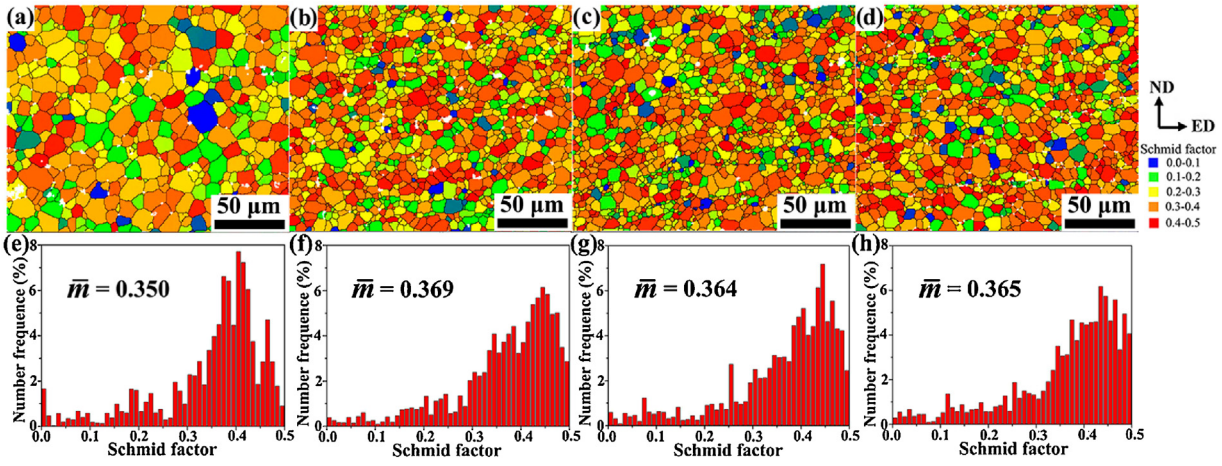

Fig. 11. Quantitative analysis of (0001)/<11−20> basal slip Schmid factor (SF) of the as-extruded alloys under tension along the ED: (a, e) TXE110 alloy; (b, f) TXE1102 alloy; (c, g) TXE1105 alloy; (d, h) TXE111 alloy.

[51]. In the current work, as seen in Fig. 2, the second phase particles in the extruded state are distributed along the ED in the form of strips, irrespective of intragranular or grain boundary. Therefore, it is reasonable to speculate that the addition of Ce increases the amount of strip distributed second phase, thereby enhancing the inhibition of twinning during compression and ultimately reducing TCA. Thirdly, texture weakening is also conducive to the improvement of TCA [52]. Correspondingly, the SF distributions for basal slip [53] under tension along the ED and {10–12} tensile twins [54] under compression along the ED are calculated, respectively, with their results shown in Figs. 11 and 12. The results manifest that the average SF for basal slip in Ce-containing alloys (0.364-0.369) is slightly higher than that in Ce-free alloy (0.350), while the corresponding tendency for {10–12} twins is opposite (Ce-free alloy: 0.295; Ce-containing alloys: 0.269-0.274). The above phenomenon implies that compared with the Ce-free alloy, the Ce-containing alloys are easier to activate basal slip in tension, and harder to activate {10–12} tensile twins in compression from the perspective of texture. Consequently, the texture weakening caused by the addition of Ce is also beneficial to the amelioration of TCA. As a result, owing to the grain refinement, the increased amount of strip distributed second phase particles and the texture weakening, the TCA of as-extruded Mg-Sn-Ca alloy is considerably improved by adding Ce.

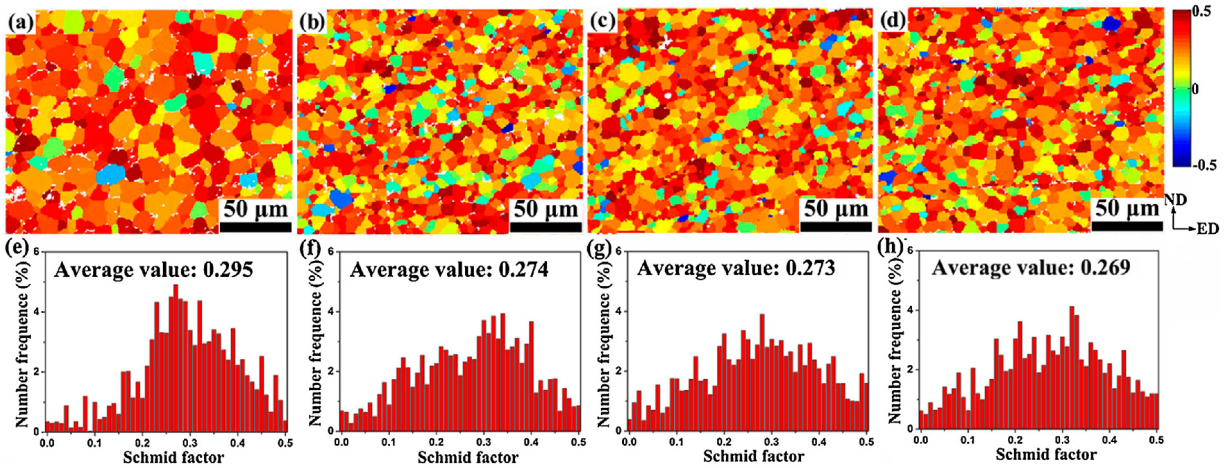

Fig. 12. Schmid factor as a function of relative spatial position and relative distributions for {10–12} twinning under compression along the ED: (a, e) TXE110 alloy; (b, f) TXE1102 alloy; (c, g) TXE1105 alloy; (d, h) TXE111 alloy. Note that a negative value of SF for {10–12} twinning would lead to contraction along the C-axes of grains and not be activated. A minus SF for {10–12} twinning is therefore treated as zero during calculation of the distribution of SFs.

5. Conclusions

(1) With the increase of Ce content, the grain size of both as-cast and as-extruded Mg-Sn-Ca alloys decreased significantly, meanwhile the second phase converted from CaMgSn to (Ca, Ce)MgSn and $Mg_{12}Ce$.

(2) The addition of Ce gave rise to texture weakening (i.e. decrease of maximum intensity and increase of tilting degree) of as-extruded Mg-Sn-Ca based alloys. The possible reason was that the volume fraction of second phase increased with rising Ce content, which aggravated the restriction on DRXed grain growth during extrusion.

(3) Actual experimental data (EBSD measurements of 10% and 20% tensile strains) in conjunction with VPSC indicated that the addition of 0.2 wt% Ce could bring about vigorously activated basal slip and homogeneous distributed tensile strain during the tensile process, and consequently contributed to the ductile improvement of Mg-Sn-Ca ternary alloy. However, the further addition of Ce (0.5 and 1.0 wt%) would deteriorate the ductility due to the coarsening of second phase particles. Besides, improved TCA performance of as-extruded Mg-Sn-Ca alloy via Ce additions could be explained by the joint effects of refined grains, increased amount of strip distributed secondary phase particles and weakened texture.

Acknowledgments

This work was financially supported by the Chongqing Science and Technology Commission (Nos. cstc2017zdcy-zdzxX0006, cstc2017jcyjAX0012 and cstc2018jcyjAX0472), the National Natural Science Foundation of China (Nos. 51531002 and U1764253), the National Key Research and Development Program of China (Nos. 2016YFB0301104 and 2016YFB0101700), the Chongqing Scientific & Technological Talents Program (No. KJXX2017002), the China Postdoctoral Science Foundation (No. 2018T110948) and the Science and Technology Research Program of Chongqing Municipal Education Commission (No. KJQN201801306).

References

[1] R.K. Sabat, A.P. Brahme, R.K. Mishra, K. Inal, S. Suwas, Acta Mater. 161 (2018) 246–257.
[2] M.G. Jiang, C. Xu, H. Yan, G.H. Fan, T. Nakata, C.S. Lao, R.S. Chen, S. Kamado, E.H. Han, B.H. Lu, Acta Mater. 157 (2018) 53–71.
[3] W.T. Jia, L.F. Ma, Q.Z. Le, C.C. Zhi, P.T. Liu, J. Alloys Compd. 783 (2019) 863–876.
[4] C.C. Zhi, L.F. Ma, Q.X. Huang, Z.Q. Huang, J.B. Lin, J. Mater. Process. Technol. 5 (2018) 1555–1561.
[5] J. Xu, B. Jiang, J.F. Song, J.J. He, P. Gao, W.J. Liu, T.H. Yang, G.S. Huang, F.S. Pan, Mater. Sci. Eng. A 732 (2018) 1–5.
[6] S.H. You, Y.D. Huang, K.U. Kainer, N. Hort, J. Magnes. Alloys 5 (2017) 239–253.
[7] D.B. Xia, G.S. Huang, S.S. Liu, A.T. Tang, S. Gavras, Y.D. Huang, N. Hort, B. Jiang, F.S. Pan, Mater. Sci. Eng. A 756 (2019) 1–10.
[8] C.Y. Zhao, X.H. Chen, F.S. Pan, S.Y. Gao, D. Zhao, X.F. Liu, Mater. Sci. Eng. A 713 (2018) 244–252.
[9] C.Y. Zhao, X.H. Chen, F.S. Pan, J.F. Wang, S.Y. Gao, T. Tu, C.Q. Liu, J.H. Yao, A. Atrens, J. Mater. Sci. Technol. 35 (2019) 142–150.
[10] F.R. Elsayed, T.T. Sasaki, T. Ohkubo, H. Takahashi, S.W. Xu, S. Kamado, K. Hono, Mater. Sci. Eng. A 588 (2013) 318–328.
[11] B.H. Kim, S.W. Lee, Y.H. Park, I.M. Park, J. Alloys Compd. 493 (2010) 502–506.
[12] T.T. Sasaki, K. Yamamoto, T. Honma, S. Kamado, K. Hono, Scr. Mater. 59 (2008) 1111–1114.
[13] W.L. Cheng, H.S. Kim, B.S. You, B.H. Koo, S.S. Park, Mater. Lett. 65 (2011) 1525–1527.
[14] Z.T. Jiang, B. Jiang, H. Yang, Q.H. Wang, J.H. Dai, F.S. Pan, J. Alloys Compd. 647 (2015) 357–363.
[15] Y.F. Chai, B. Jiang, J.F. Song, Q.H. Wang, J.J. He, J. Zhao, G.S. Huang, Z.T. Jiang, F.S. Pan, Mater. Sci. Eng. A 730 (2018) 303–316.
[16] H.C. Pan, G.W. Qin, Y.M. Huang, Y.P. Ren, X.C. Sha, X.D. Han, Z.Q. Liu, C.F. Li, X.L. Wu, H.W. Chen, C. He, L.J. Chai, Y.Z. Wang, J.F. Nie, Acta Mater. 149 (2018) 350–363.
[17] A.Y. Zhang, R. Kang, L. Wu, H.C. Pan, H.B. Xie, Q.Y. Huang, Y.J. Liu, Z.R. Ai, L.F. Ma, Y.P. Ren, G.W. Qin, Mater. Sci. Eng. A 754 (2019) 269–274.
[18] Y.Z. Du, X.G. Qiao, M.Y. Zheng, K. Wu, S.W. Xu, Mater. Sci. Eng. A 620 (2015) 164–171.
[19] Y.Z. Du, M.Y. Zheng, X.G. Qiao, D.B. Wang, W.Q. Peng, K. Wu, B.L. Jiang, Mater. Sci. Eng. A 656 (2016) 67–74.
[20] T. Laser, C. Hartig, M.R. Nürnberg, D. Letzig, R. Bormann, Acta Mater. 56 (2008) 2791–2798.
[21] M.B. Yang, F.S. Pan, L. Cheng, J. Shen, Mater. Sci. Eng. A 512 (2009) 132–138.
[22] M.B. Yang, Y.L. Ma, F.S. Pan, Trans. Nonferrous Met. Soc. China 19 (2009) 1087–1092.
[23] C. Tomé, G.R. Canova, U.F. Kocks, N. Christodoulou, J.J. Jonas, Acta Metall. 32 (1984) 1637–1653.
[24] R.A. Lebensohn, C.N. Tomé, Acta Metall. Mater. 41 (1993) 2611–2624.
[25] A. Molinari, G.R. Canova, S. Ahzi, Acta Metall. 35 (1987) 2983–2994.
[26] L.Y. Zhao, A. Chapuis, Y.C. Xin, Q. Liu, J. Alloys Compd. 710 (2017) 159–165.
[27] J. Sun, L. Jin, Dong S, J. Dong, Z.Y. Zhang, F.H. Wang, W.J. Ding, A.A. Luo, Mater. Des. 122 (2017) 164–171.
[28] W.J. Ren, R.L. Xin, J.B. Xu, B. Song, L. Zhang, Q. Liu, J. Alloys Compd. 792 (2019) 610–616.
[29] Y.F. Chai, B. Jiang, J.F. Song, Q.H. Wang, H. Gao, B. Liu, G.S. Huang, D.F. Zhang, F.S. Pan, J. Alloys Compd. 782 (2019) 1076–1086.
[30] Y.F. Chai, B. Jiang, J.F. Song, B. Liu, G.S. Huang, D.F. Zhang, F.S. Pan, Mater. Sci. Eng. A 746 (2019) 82–93.
[31] A. Kozlov, J. Gröbner, R. Schmid-Fetzer, J. Phase Equilib. Diff. 35 (2014) 502–517.
[32] M. Celikin, R. Gauvin, M. Pekguleryuz, Mater. Sci. Eng. A 719 (2018) 199–205.
[33] N. Stanford, Mater. Sci. Eng. A 528 (2010) 314–322.
[34] H.L. Ding, X.B. Shi, Y.Q. Wang, G.P. Cheng, S. Kamado, Mater. Sci. Eng. A 645 (2015) 196–204.

[35] Y. Ali, D. Qiu, B. Jiang, F.S. Pan, M.X. Zhang, J. Alloys Compd. 619 (2015) 639–651.
[36] Y. Jiang, Y.A. Chen, J.J. Gao, Mater. Des. 105 (2016) 34–40.
[37] W.L. Xiao, S.S. Jia, J. Wang, Y.M. Wu, L.M. Wang, Mater. Sci. Eng. A 474 (2008) 317–322.
[38] L. Shang, I.H. Jung, S. Yue, R. Verma, E. Essadiqi, J. Alloys Compd. 492 (2010) 173–183.
[39] C.D. Barrett, A. Imandoust, A.L. Oppedal, K. Inal, M.A. Tschopp, H. El Kadiri, Acta Mater. 128 (2017) 270–283.
[40] H.M. Yin, B. Jiang, X.Y. Huang, Y. Zeng, Q.S. Yang, M.X. Zhang, F.S. Pan, Trans. Nonferrous Met. Soc. China 23 (2013) 1936–1941.
[41] J. Bohlen, S.B. Yi, D. Letzig, K.U. Kainer, Mater. Sci. Eng. A 527 (2010) 7092–7098.
[42] K. Hantzsche, J. Bohlen, J. Wendt, K.U. Kainer, S.B. Yi, D. Letzig, Scr. Mater. 63 (2010) 725–730.
[43] J.P. Hadorn, K. Hantzsche, S.B. Yi, J. Bohlen, D. Letzig, J.A. Wollmershauser, S.R. Agnew, Metall. Mater. Trans. A 43 (2012) 1347–1362.
[44] S.W. Lee, S.H. Kim, W.K. Jo, W.H. Hong, W. Kim, B.G. Moon, S.H. Park, J. Alloys Compd. 791 (2019) 700–710.
[45] Q.H. Wang, Y.Q. Shen, B. Jiang, A.T. Tang, Y.F. Chai, J.F. Song, T.H. Yang, G.S. Huang, F.S. Pan, Mater. Sci. Eng. A 736 (2018) 404–416.
[46] S.W. Xu, K. Oh-Ishi, H. Sunohara, S. Kamado, Mater. Sci. Eng. A 558 (2012) 356–365.
[47] H.X. Wang, L.X. Zhang, W.Z. Chen, D.Q. Fang, W.C. Zhang, G.R. Cui, Mater. Sci. Eng. A 736 (2018) 239–247.
[48] S.W. Bae, S.H. Kim, J.U. Lee, W.K. Jo, W.H. Hong, W. Kim, S.H. Park, J. Alloys Compd. 766 (2018) 748–758.
[49] B. Kim, S.M. Baek, H.Y. Jeong, J.G. Lee, S.S. Park, J. Alloys Compd. 660 (2016) 304–309.
[50] S.H. Kim, S.H. Park, Mater. Sci. Eng. A 733 (2018) 285–290.
[51] T. Homma, N. Kunito, S. Kamado, Scr. Mater. 61 (2009) 644–647.
[52] G.G. Wang, G.S. Huang, X. Chen, Q.Y. Deng, A.T. Tang, B. Jiang, F.S. Pan, Mater. Sci. Eng. A 705 (2017) 46–54.
[53] D.B. Xia, G.S. Huang, Q.Y. Deng, B. Jiang, S.S. Liu, F.S. Pan, Mater. Sci. Eng. A 715 (2018) 379–388.
[54] D.B. Xia, X. Chen, G.S. Huang, B. Jiang, A.T. Tang, H. Yang, S. Gavras, Y.D. Huang, N. Hort, F.S. Pan, Scr. Mater. 171 (2019) 31–35.